



Triaxial compression behavior of large-scale jointed coal: a numerical study

Xiaoqing Wang^{1,2,3} · Fuqiang Gao^{1,2,3}

Received: 13 April 2021 / Accepted: 2 August 2022
© The Author(s) 2022

Abstract

Accurate estimation of the triaxial compression behavior of jointed coal is essential for coal mining. Few studies addressed the triaxial compression behavior of large-scale rock mass, especially with real joint geometry. We employed a numerical synthetic rock mass (SRM) method to study the triaxial compression behavior of jointed coal. Jointed-coal specimens were constructed based on in-situ joint measurements and microparameter calibration against laboratory experiments. A series of triaxial compression tests under different loading orientations and confining pressures were numerically performed to obtain joint and confining-pressure effects on the triaxial compression behavior and reveal the failure mechanism of jointed coal. Results suggest that the triaxial compression behavior of the jointed coal has strong joint and confining-pressure effects. Joints weaken the strength and elastic modulus, reduce the lateral deformation, and affect the geometries of the shear-rupture surface. An increase in the confining pressure causes the peak and residual strength increase significantly. With an increase in the confining pressure, the elastic modulus increases sharply at low confining pressure, the mechanical behavior transitions from brittleness to ductility, the failure mode transitions from shear-rupture surface to plastic flow, and the joint effect diminishes and even disappears. The jointed coal fails by means of a shear-rupture surface under triaxial compression loading with a confining pressure (which is not too high), and the geometries of the shear-rupture surface vary with the distribution of joints.

Keywords Jointed coal · Triaxial compression · Synthetic rock mass · Failure mode

1 Introduction

Coal joints exert significant influence on the stability and gas flow of coalbeds. Literature on coal joints dates back to the early nineteenth Century (Kendall and Briggs 1933). Most current investigations on coal joints focus on the development of coal bed methane, while few refer to the stability analysis of coal mining. Coal joints are consistently classified into three categories: bedding planes, endogenetic joints, and exogenetic joints (Kang et al. 1994). Bedding planes are the most common coal joints and tend to cause

roof separation of roadways in coal mining (Wang et al. 2016). Exogenetic joints result from tectonic movements and always appear in groups. Endogenetic joints are formed during the coalification stage (Laubach et al. 1998; Su et al. 2001). Cleats, which is the common term for endogenetic joints (Dron 1925), usually occur in two sets: face and butt cleats. In most instances, the two sets of cleats are perpendicular and perpendicular to the bedding planes. The butt cleats are located between adjacent face cleats, while the face cleats are more continuous and larger. Laubach et al. (1998) provided a schematic illustration of the coal-cleat geometry and pointed out that cleats along with bedding planes cut jointed coal into cube-shaped blocks.

Coal masses occur under three-dimensional stress states. Therefore, it is essential to accurately estimate the triaxial compression behavior of coal mass containing joints in coal mining, which is also the challenge for mining engineers. The Hoek–Brown failure criterion based on rock-mass classification is commonly used to estimate the rock-mass properties (Hoek and Brown 1980, 1997). However, rock-mass

✉ Fuqiang Gao
fuqgao@gmail.com

¹ CCTEG Coal Mining Research Institute, Beijing, China

² Mining & Designing Branch, China Coal Research Institute, Beijing, China

³ State Key Laboratory of Coal Mining and Clean Utilization (China Coal Research Institute), Beijing, China

classification methods, including the Q Index (Barton et al. 1974), RMR system (Bieniawski 1973), and geological strength index (Hoek 1994), may be subjective. Laboratory and field tests are used widely, however, they suffer from some insurmountable limitations. Specimens that contain a single joint or a simple layout of joints are prepared in laboratory tests (Xiao et al. 2015; Yang et al. 2018; Walton et al. 2018; Dou et al. 2021; Kim et al. 2021), which do not represent the real highly fractured rock mass. This difficulty is alleviated by the application of 3D printing technology in the preparation of highly jointed specimens (Head and Vanorio 2016; Jiang et al. 2016; Jiang and Song 2018), but has not been resolved. Field tests of uniaxial compression on coal mass have been conducted by Bieniawski (1968a, b); Cook et al. (1971), Van Heerden (1975) to optimize the coal-pillar size. However, field tests have rarely been conducted because of their high cost and complicated operation.

The vast improvement in desktop computing power has led to the increasingly widespread employment of numerical simulation methods. In the continuum approach, the rock mass is assumed as an equivalent continuum, which follows a constitutive law. In a discrete approach, the rupture behavior of the rock mass can be simulated by block-based codes, including UDEC, 3DEC, and DDA, and particle-based codes, such as PFC, EDEM, and Yade. The synthetic rock mass (SRM) approach based on PFC appeared in 2007 as a step forward in the parametric research of the rock mass (Ivars et al. 2011). The SRM approach integrates the intact-rock model with the joint-geometry model to represent the real jointed rock mass, and thus, can simulate initiation, propagation, and coalescence of matrix fractures, and slip along and the opening of pre-existing joints. Compared with block-based discrete methods, the model in the SRM approach is more representative of the rock and iterates based on relatively simple particle-contact laws rather than more complex constitutive laws (Itasca Consulting Group Inc. 2016), which proves better for the investigation of the rupture mechanism of intact and jointed rock. Numerous researchers successfully employed the SRM approach to investigate the triaxial compression behavior of the rock mass (Zhou et al. 2014; Huang et al. 2016; Chen et al. 2021), which proves that the SRM approach is capable of investigating the triaxial compression behavior of jointed coal.

Although numerous studies have been reported on the triaxial compression behavior of jointed rock using laboratory tests and the SRM approach, most were limited to a simplified rock mass with only a single joint or a small number of arranged joints. Few reports exist in the literature on triaxial compression behavior for a real highly jointed rock mass, especially at large scales. Therefore, we constructed jointed-coal specimens that contain a real layout of joints based on an in-situ joint measurement and microparameter

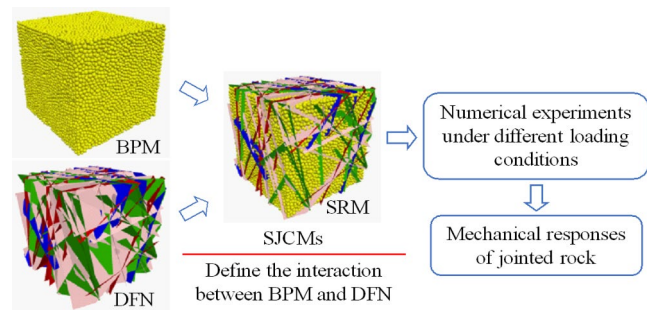


Fig. 1 Process of SRM approach

calibration against laboratory experiments using the SRM approach. We conducted a series of triaxial compression tests under different loading orientations and confining pressures numerically on SRM specimens with a representative element volume (REV) size to obtain joint and confining-pressure effects on the triaxial compression behavior of jointed coal. Hence, we reveal the failure modes and mechanisms of jointed coal subjected to triaxial compression.

2 Preparation of SRM specimen for jointed coal

2.1 SRM approach

In PFC, the intact rock is represented by an assembly of separate particles bonded together, called the bonded particle model (BPM) (Potyondy and Cundall 2004). The parallel-bond contact model (PBCM) (Itasca Consulting Group Inc. 2016) provided in PFC is chosen to construct the BPM when modeling intact rock. A discrete fracture network (DFN) is generated using a Monte-Carlo simulation based on joint data from outcrop/excavation mapping and borehole logging to represent joints geometry in real jointed rock. The SRM approach employs a DFN superimposed upon a BPM to represent a jointed rock mass. The smooth-joint contact model (SJCMS) provided in PFC is used to define the interaction between BPM and DFN in the SRM approach, whereby the SJCMS are assigned to all contacts (originally bonded by PBCMs) between particles on opposite sides of the DFN. The process of the SRM approach is presented in Fig. 1.

2.2 Preparation of jointed-coal SRM specimen

2.2.1 Joints sampling for jointed coal

A joint-sampling campaign on the No.3 coal seam was performed at the Sihe coal mine, Shanxi, China. Scan lines and a scan window were set up on the two side surfaces and the top surface in a 4 m × 4 m × 4 m drilling field to cover all sets

Table 1 Statistical results of coal-joint data used for DFN generation

Joint set	Distribution (mean value / standard deviation)			
	Dip	Dip direction	Trace	Spacing
Bedding planes	N/A	N/A	N/A	NE (0.14/0.14)
Butt cleats	Normal (90/0.30)	Normal (90/0.20)	NE (0.28/0.28)	Log-normal (0.11/0.24)
Face cleats	Normal (90/0.30)	Normal (180/0.20)	Normal (2.80/0.20)	Log-normal (0.16/0.59)

Note: (1) NE means negative exponential; (2) trace for butt cleats and face cleats only refers to length trace, and the width trace is equivalent to the spacing of bedding planes

of joints. Finally, a total of 119 joints, including 28 bedding planes, 51 butt cleats, and 40 face cleats were mapped. The dip, dip direction, size, and spacing were analyzed statistically for each set, as given in Table 1.

2.2.2 Construction and calibration of coal DFN

The coal DFN was first generated in code FracMan using the statistical results in Table 1 and then imported into PFC3D by a series of data processing (Fig. 2b). The spatial distribution of bedding planes, face cleats, and butt cleats in coal DFN agrees well with what is depicted in the coal mass (Laubach et al. 1998; Su et al. 2001). The measured and numerical rock quality designations (RQDs) for two boreholes (Fig. 2b) were compared to calibrate the coal DFN. The numerical RQD is obtained by counting the sum of the lengths of borehole segmentations cut by the DFN that are longer than 10 cm with respect to the entire borehole length in a developed Fish program. The RQD values of the two methods are similar (89.2% vs. 88.8% for one borehole, and 85.2% vs. 82.0% for the other borehole), which indicates that the generated DFN can represent the real joint geometry in jointed coal.

Fig. 2 Construction of jointed-coal SRM specimen: **a** Coal BPM; **b** 4 m × 4 m × 4 m coal DFN; **c** Inserting BPM into DFN; **d** Close-up view of jointed-coal SRM specimen with REV size

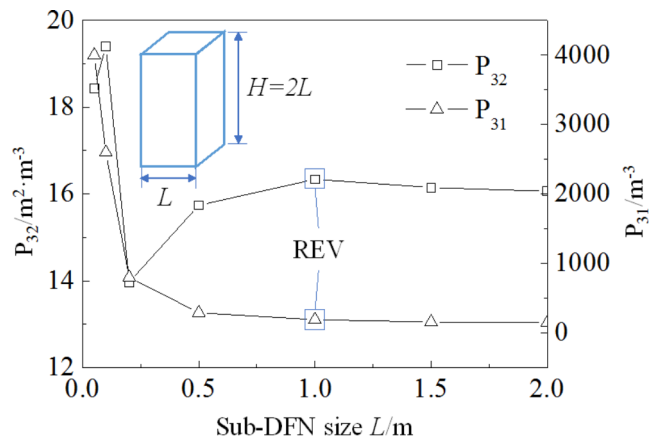
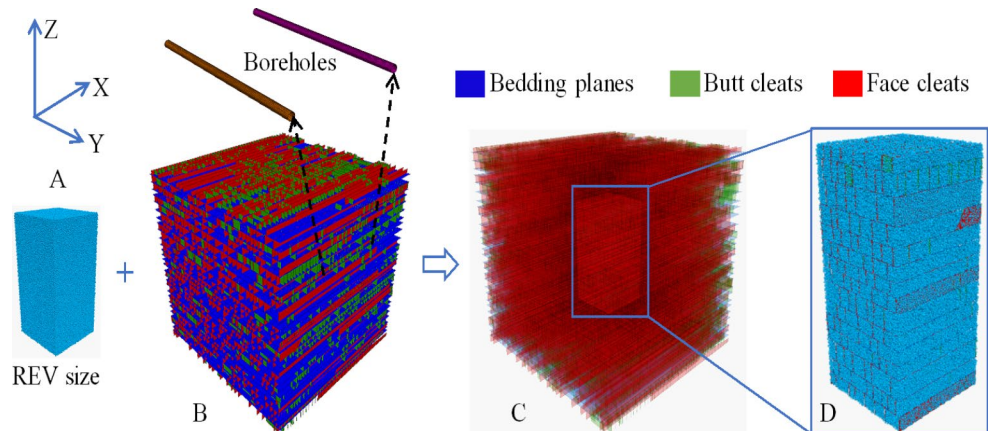


Fig. 3 Varieties of P_{32} and P_{31} with respect to the sub-DFN size

2.2.3 REV determination for jointed coal

The coal mass exhibits a strong scale effect, whereby the strength decreases with the sample size until the representative element volume (REV) is reached (Bieniawski 1968a, b). The REV can be estimated by evaluating the variety of joint intensity. P_{32} and P_{31} are used as joint-intensity indexes, which refer to the joint area and joint number in the unit rock-mass volume, respectively. Here, P_{32} and P_{31} are calculated with different sizes of sub-DFNs based on a cuboid with an aspect ratio of 2:1 by developing a PFC3D Fish program. In the Fish program, the sub-DFNs are intercepted randomly five times for each size in the jointed-coal DFN to reduce the discretization, and an average value is calculated for P_{32} and P_{31} . The varieties of P_{32} and P_{31} with the size of sub-DFNs are shown in Fig. 3. P_{32} and P_{31} tend to be steady when the sub-DFN size increases to 1.0 m × 1.0 m × 2.0 m, the size of which is identified as the REV for jointed coal. The REV of jointed coal is consistent with the field observation where the REV of coal is 1.0–1.5 m. (Bieniawski 1968a, b).

Table 2 Calibrated microparameters for PBCMs and SJCMs in jointed-coal specimen

Ball parameter	Value	PBCM parameter	Value	SJCM parameter	Value
Density (kg/m ³)	2500	Cohesion (MPa)	8.0	Normal stiffness, \bar{k}_{nj} (GPa/m/m)	30
R_{min} (cm)	0.8	S.D. Cohesion (MPa)	1.5	Shear stiffness, \bar{k}_{sj} (GPa/m/m)	6
R_{max} (cm)	1.0	Tensile strength (MPa)	4.0	Coefficient of friction	0.577
Porosity	0.2	S.D. Tensile strength (MPa)	1.5	Tensile strength (MPa)	0
Coefficient of friction, μ	0.7	Angle of internal friction (°)	0	Cohesion (MPa)	0
k_n/k_s	5.0	\bar{k}_n/\bar{k}_s	5.0		
E_c (GPa)	1.8	\bar{E}_c (GPa)	1.8		

S.D.: Standard deviation

2.2.4 Construction and calibration of jointed-coal specimen with REV size

Considering the SJCMs, the particle size must be sufficiently small to reproduce slip along joints and rock-bridge breakage (Ivars et al. 2011), and more than five particles must exist between adjacent joints (Gao et al. 2014). The particle diameter for coal BPM is determined as 1.6–2.0 cm, because the minimum spacing between joints in constructed DFN is 10.0 cm. To increase the construction efficiency of coal BPM, the 0.5 m cubic periodic brick (Itasca Consulting Group Inc. 2016) was generated first and then assembled into the REV-sized BPM. The REV-sized BPM consists of 518,432 particles bonded by PBCMs, which is a large number for particle-based DEM simulation. The BPM is inserted into the DFN at any position, after which the SJCMs are assigned to all contacts intercepted by the DFN to substitute the PBCMs, thus creating the jointed-coal SRM specimen (Fig. 2).

The calibration of microparameters for PBCMs and SJCMs is required prior to numerical analysis. For PBCMs calibration, some uniaxial compression laboratory tests on intact coal specimens were conducted to obtain macro properties. A cylindrical BPM was constructed in PFC3D and used to produce the targeted macro properties from the laboratory tests by selecting microparameters by trial and error. To calibrate the SJCMs, a series of direct shear laboratory tests on coal specimens with a single-through joint under different normal stresses was carried out to obtain the macro properties of coal joint. The same numerical model was generated and used to conduct direct shear numerical tests to achieve the same macro properties from the laboratory

tests. The detailed calibration for PBCMs and SJCMs in the jointed-coal SRM specimen are referred to in the authors' previous paper (Wang et al. 2019). The calibrated microparameters for balls, PBCMs, and SJCMs in jointed-coal SRM specimens are listed in Table 2.

2.3 Rupture-analysis method for SRM specimen

BPM damage is represented by shear and tension breakage of bonds that result in shear and tension microcracks, respectively. The initiation, propagation, and coalescence of these microcracks form matrix fractures, which either have a tension or shear mechanism. A discrimination method for the macroscopic formation mechanism of matrix fractures was proposed, which is in contrast to the comparison of velocity or displacement vectors of particles on the sides of a matrix fracture by Bewick et al. (2014). If a matrix fracture is composed of only tension microcracks and opens a large gap, the macro formation mechanism is considered as tension. If a matrix-fracture is composed of tension and shear microcracks and closes, the macro formation mechanism can be judged as shear, as shear always occurs between two conterminous objects accompanied by the tension breakage of asperities (Bahaaddini et al. 2013). With a large gap, the open fractures can be displayed easily and clearly by means of cut planes. For the closed fractures, microcracks can be used to depict the fracture geometry, whereas this does not work when the closed fractures are heavily distributed. Particles on opposite sides of the closed fracture contact each other and form linear contact models (LCMs, a basic unbonded contact model provided in code PFC (Itasca Consulting Group Inc. 2016)) in the sliding process, such that the LCMs can be used to display the closed fractures.

Fractures in the SRM specimen are generally composed of activated joints and matrix fractures. Activated joints result from joints activation (tension or shear breakage of pre-existing joints), which can be quantified by the reduced number of SJCMs in the SRM approach. Therefore, the joints activation ratio was proposed to evaluate the contribution of pre-existing joints on the failure of SRM specimens.

$$m = \frac{\Delta N_{\text{SJCM}}}{N_{\text{SJCM}}} \quad (1)$$

where, m is joints activation ratio; ΔN_{SJCM} is the reduced number of SJCMs, and N_{SJCM} is the initial number of SJCMs.

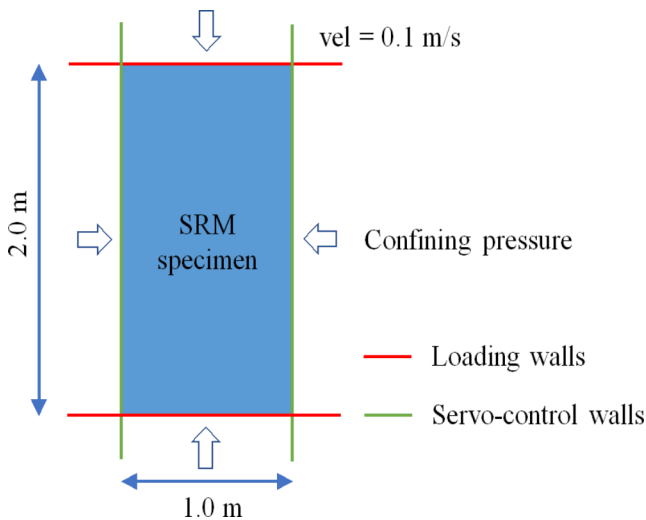


Fig. 4 Schematic of numerical model used to perform triaxial compression test

3 Numerical triaxial compression tests of jointed coal

3.1 Setup of numerical model under triaxial compression

The schematic of a triaxial test on the SRM specimen under constant confining pressure is presented in Fig. 4. The top and bottom walls act as loading plates, and the lateral walls are used to maintain a constant confining pressure using a servo-control mechanism (Itasca Consulting Group Inc. 2016). All walls are 0.2 times larger than the SRM specimen. All sides of the SRM specimen are loaded first into the targeted confining pressure using a servo-control mechanism. Then, a velocity of 0.1 m/s is applied to the loading walls to initiate the triaxial test, while the lateral confining pressures are kept constant through servo-control walls during the test. Sensitivity studies showed that this loading rate is sufficiently slow to ensure that the specimen remains in a quasi-static equilibrium. The axial stress is obtained by dividing the average recorded reaction force on the loading walls by the cross-sectional area of the SRM specimen. The axial strain is calculated as the ratio of the sum of the displacement of both loading walls to the initial height of the SRM specimen. The lateral strain has a similar calculation method.

All triaxial compression numerical tests were conducted using code PFC3D 5.0 on a 64-bit, two 2.30 GHz Intel(R) Xeon(R) processor computer with 64.0 GB RAM. Each case took 2–15 days to complete the calculations due to the large number of particles used. The calculation time increases sharply with confining pressure, because a large number of

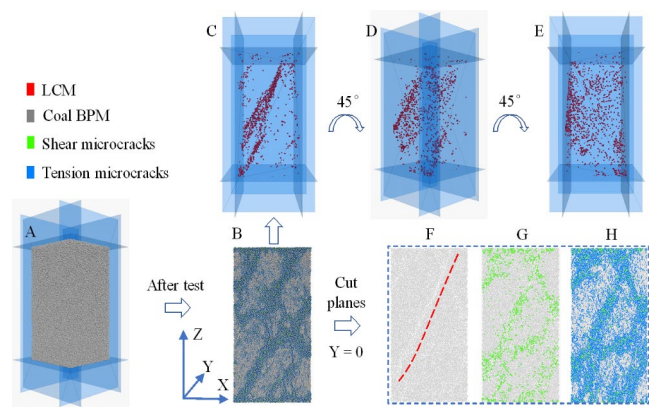


Fig. 5 Numerical results of fracture geometry and microcracks distribution for intact coal with REV size after triaxial compression test

microcracks grow and adjust their locations and orientations frequently in the calculation under high confining pressure.

3.2 Numerical triaxial compression tests under different loading orientations

3.2.1 Numerical triaxial compression test on intact coal with REV size

The numerical model of triaxial compression for coal BPM with a REV size is illustrated in Fig. 5a. After triaxial compression under a 1 MPa confining pressure, the specimen retains integrity, except for some microcrack bands along the surface (Fig. 5b). As illustrated in the cut planes (Fig. 5f, g, and h) at the $Y=0$ position, the microcrack bands form a cut-through fracture labeled by the red dotted line, which is closed and composed of tension and shear microcracks. According to the rupture-analysis method in Sect. 2.3, the fracture is a shear-rupture surface. For a clear display, the shear-rupture surface denoted by LCMs is extracted and rotated twice (Fig. 5c, d, and e). The shear-rupture surface is of an approximate parallelogram with a missing corner. The total number of microcracks is 1,225,010, of which 1,072,842 are tensile microcracks, and 152,168 are shear microcracks.

The curves of the axial stress difference, confining pressure, and lateral strain against axial strain are plotted in Fig. 6. The confining pressures fluctuate around 1 MPa, which indicate a good servo control on the lateral walls. The stress difference refers to the difference between the monitored axial stress and targeted confining pressure. The pre-peak curve of stress difference remains relatively straight, and the post-peak curve drops rapidly to a steady condition, with an elastic modulus of 2.36 GPa, a triaxial compression strength (TCS) of 33.7 MPa, and residual strength of 10.3 MPa. The lateral strain increases sharply after the peak strength, stabilizes briefly at the residual strength stage, and

Fig. 6 Numerical results of stress and strain for intact coal with REV size after triaxial compression test

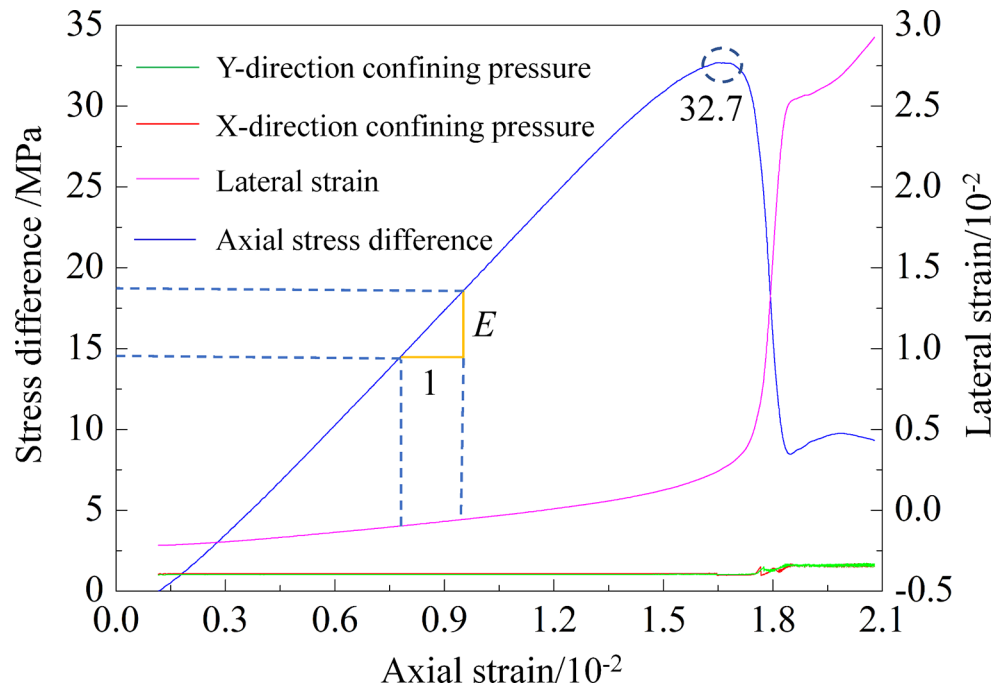
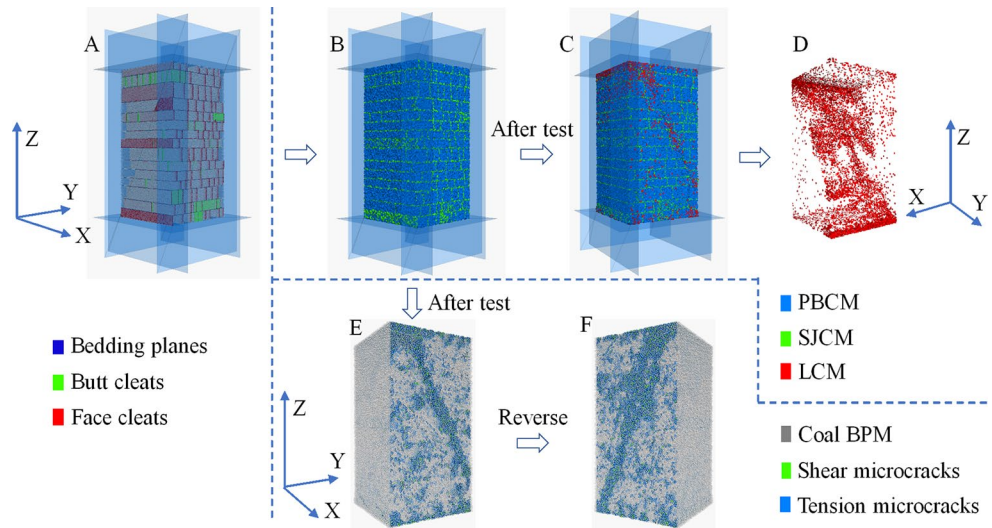


Fig. 7 Joint geometry and rupture surface for jointed coal with REV size subjected to numerical triaxial compression with loading perpendicular to bedding planes



exhibits a rapidly increasing trend, with a Poisson’s ratio of 0.23.

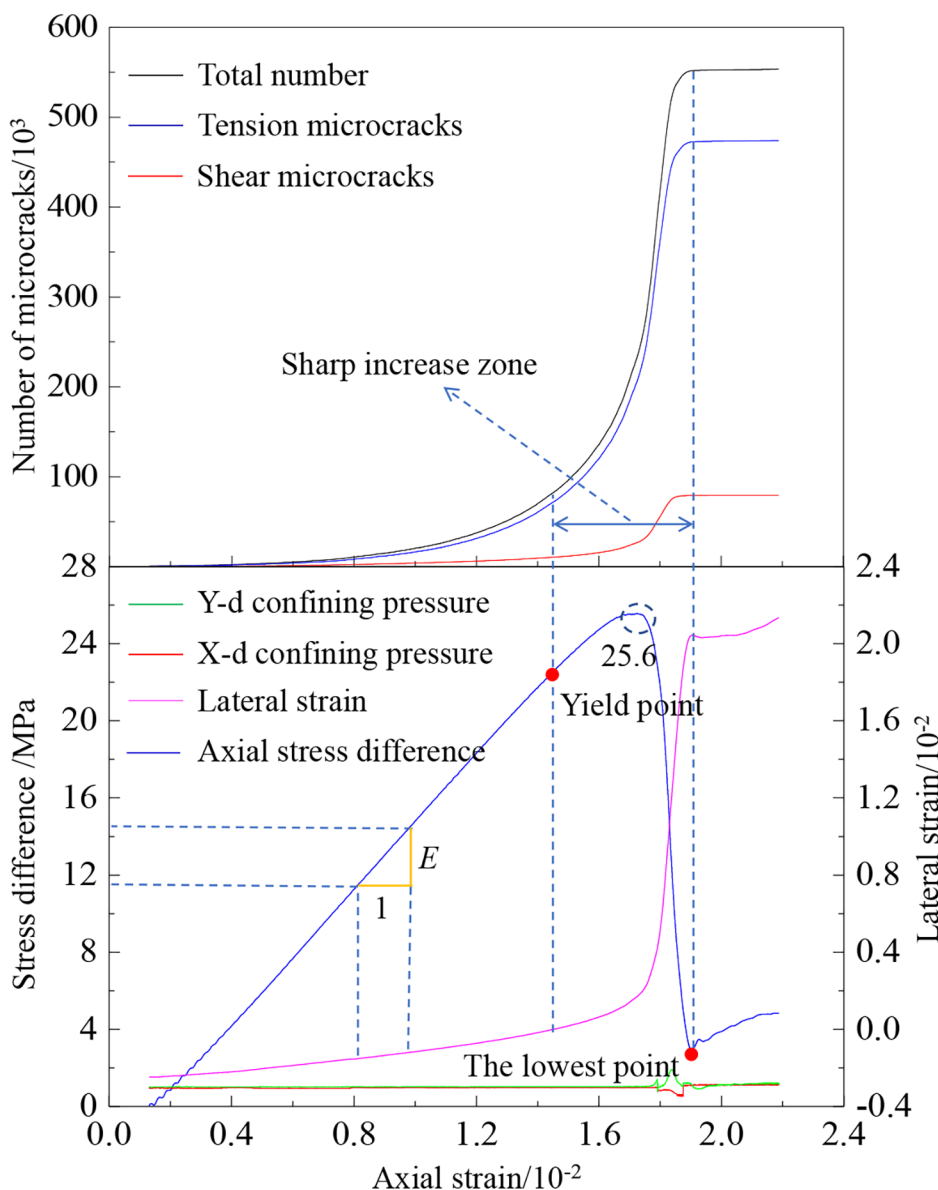
3.2.2 Numerical test on jointed coal with loading perpendicular to bedding planes

The SRM specimens of jointed coal to be loaded perpendicular to the bedding planes are presented in Fig. 7a (joints geometry) and b (contact models). After the triaxial test, no open fractures grow, but an inclined band that consists of tension and shear microcracks cuts through the specimen (Fig. 7e and f). The same inclined band of the LCMs that corresponds to the microcrack band also appears in the final contact models (Fig. 7c), which is extracted and shown

in Fig. 7d. According to the rupture-analysis method, the inclined band depicts the shear-rupture surface, which is a parallelogram.

The curves of the microcrack number, axial stress difference, confining pressure, and lateral strain against axial strain are plotted in Fig. 8. Owing to a good servo control on lateral walls, the confining pressures fluctuate around 1 MPa. In the pre-peak stage, the mechanical behavior of specimen transits gradually from elasticity to plasticity with the increase in axial stress, which produces the yield point. The sharp increase zone of the microcrack curves ranges from the yield point to the lowest point, where the coal matrix breaks heavily and results in a rapid growth of the microcrack number. In the post-peak stage, the number

Fig. 8 Numerical results of stress and strain for jointed coal after triaxial compression with loading perpendicular to bedding planes. *Y*-d and *X*-d refer to the *Y*- and *X*-directions, respectively



of microcracks does not increase, but the lateral strain still increases, which indicates that the lateral deformation of the specimen originates from the increase in the gap of the existing fractures, rather than the formation of new fractures. The TCS, elastic modulus, Poisson’s ratio, and residual strength are 26.6 MPa, 1.78 GPa, 0.20, and 4.0 MPa, respectively.

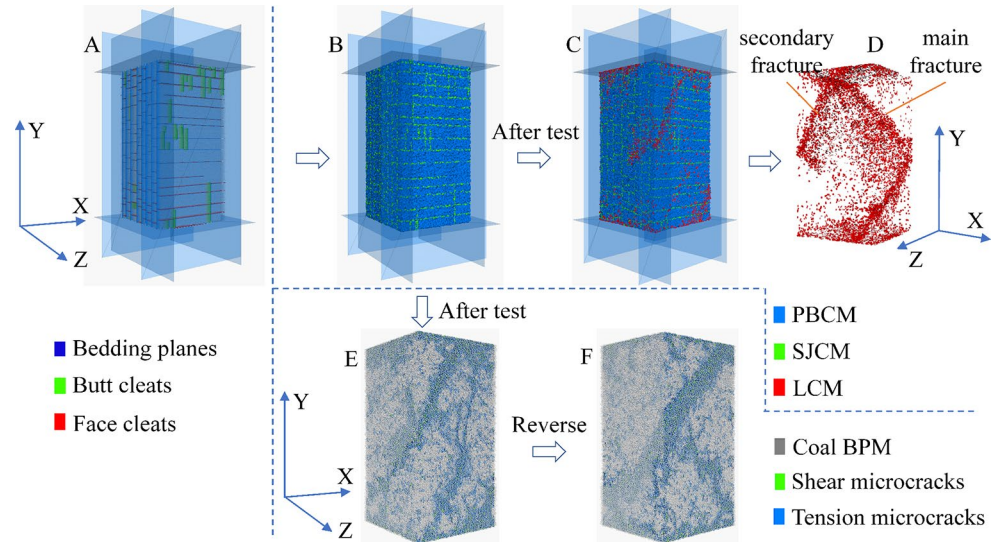
3.2.3 Numerical test on jointed coal with loading perpendicular to face cleats

The SRM specimen of jointed coal to be compressed triaxially perpendicular to the face cleats is presented in Fig. 9a. The corresponding contact model geometry is displayed in Fig. 9b. After the test, some LCMs were added to the specimen (Fig. 9c), which are extracted for a clear display

in Fig. 9d. The distribution of microcracks agrees well with the LCMs (Fig. 9e and f), indicating that closed fractures result from triaxial compression. According to the rupture-analysis method for SRM specimens, bands of the linear-contact model reveal a shear-rupture surface. The geometry of shear-rupture surface differs from that under triaxial compression with loading perpendicular to the bedding planes and is composed of a main fracture and a secondary fracture (Fig. 9d).

The curves of stress, strain, and microcrack number are plotted in Fig. 10. The steady confining pressures indicate good servo control on the lateral walls. The TCS is 26.8 MPa at a confining pressure of 1 MPa, with an elastic modulus of 1.75 GPa and a Poisson’s ratio of 0.18. The sharp increase in the microcrack number spans from the yield point to the

Fig. 9 Joint geometry and rupture surface for jointed coal with REV size subjected to numerical triaxial compression with loading perpendicular to face cleats



lowest point in the curve of the axial stress difference, where the coal matrix breaks heavily. In the residual strength stage, the axial stress is stable, but the lateral strain increases sharply. The microcrack number increases, which means that the lateral deformation results mainly from the increase in gap of the existing fractures, and the formation of new fractures contributes. The residual strength is 7.9 MPa.

3.2.4 Numerical test on jointed coal with loading perpendicular to butt cleats

The joint geometry in the SRM specimen to be triaxially compressed perpendicular to the butt cleats is shown in Fig. 11a, and the corresponding contact model geometry is presented in Fig. 11b. After the test, some microcrack bands that consisted of tension and shear microcracks cross through the specimen surface (Fig. 11e and f). This situation is the same as the two situations above, and numerous LCMs appear in the contact model geometry (Fig. 11c). These LCMs depict the geometry of the shear-rupture surface, which is extracted for clear display (Fig. 11d). The shear-rupture surface approximates a diamond.

The numerical results are shown in Fig. 12. Similar to the scenario with triaxial compression perpendicular to the bedding planes and face cleats, the sharp increase in microcrack number ranges from the yield point to the lowest point in the curve of axial stress difference. The lateral deformation still increases significantly in the residual strength stage. The TCS, elastic modulus, Poisson's ratio, and residual strength are 26.1 MPa, 1.89 GPa, 0.21, and 8.5 MPa, respectively.

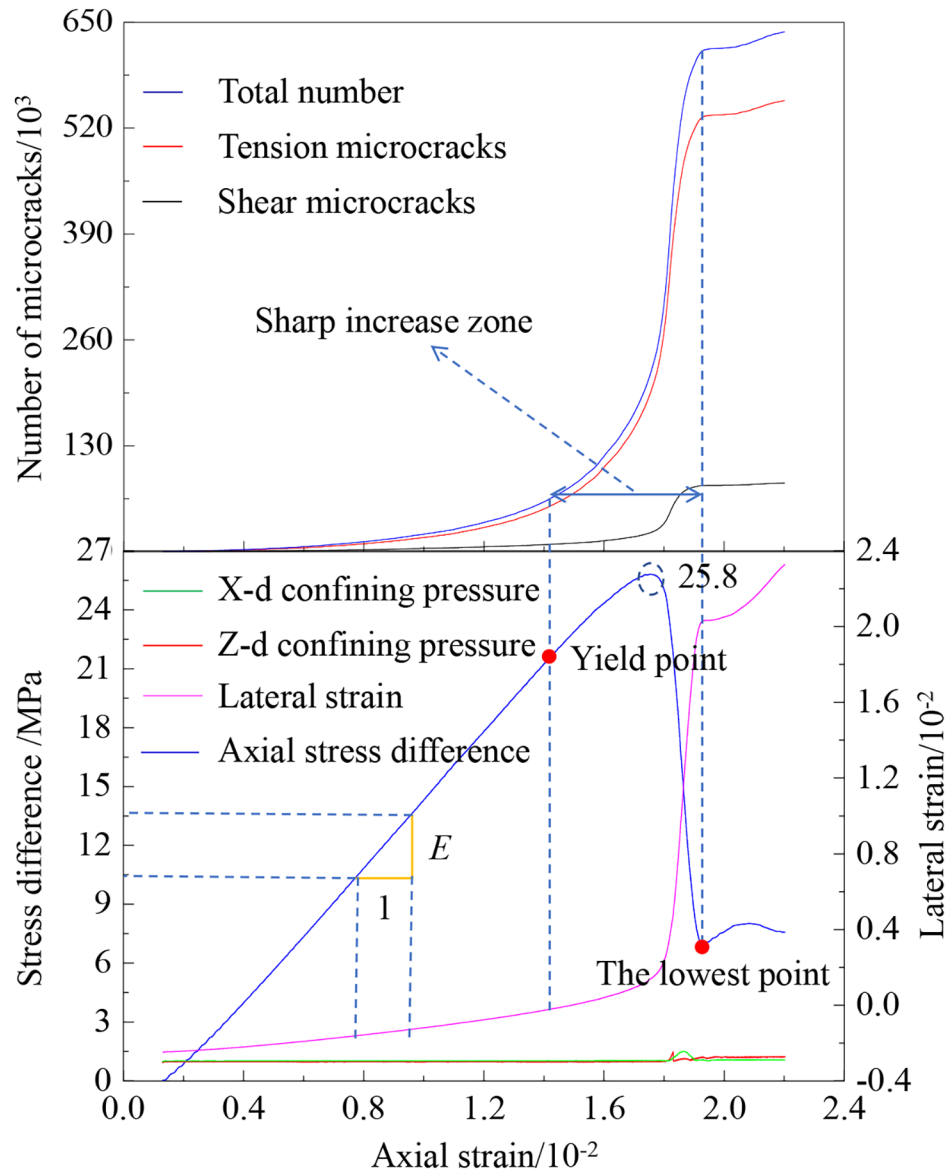
3.3 Numerical triaxial compression tests under different confining pressures

A series of numerical triaxial compression tests on jointed coal under different confining pressures were performed to investigate the confining-pressure effect. Based on the jointed-coal SRM specimen with loading perpendicular to the butt cleats (Fig. 11a), four different confining pressures, namely, 0, 1, 5, and 10 MPa were applied.

The fracture geometries under different confining pressures are shown in Fig. 13. Without a confining pressure (i.e., the loading is a uniaxial compression test), fractures initiated and propagated along the joints parallel to the loading direction after loading (Fig. 13a). Wing cracks are generated at the ends of the activated joints. When the confining pressure increases to 1 and 5 MPa, the inclined shear-rupture surfaces appear in the specimen, whereas the shapes of shear-rupture surfaces are different. When the confining pressure is 1 MPa, the shape is a flat-bottomed rhombus (Fig. 13b), while when the confining pressure is 5 MPa, the shape is a diagonal rhombus (Fig. 13c). Numerous microcracks exist over the specimen at 10 MPa confining pressure, which indicates that the jointed-coal specimen is ruptured by plastic flow (Fig. 13d).

The numerical strength results under different confining pressures are shown in Fig. 14. As illustrated in Fig. 14, the TCS is low, and the residual strength is close to zero without a confining pressure. When the confining pressure increases to 1 MPa, the TCS and residual strength increase significantly, but the axial stress drops sharply in the post-peak stage, which indicates brittle behavior for jointed coal. When the confining pressure increases to 5 MPa, the TCS and residual strength also increase. The peak zone becomes smooth and wide, and the axial stress decreases gently, which shows a transition from brittleness to ductility. When

Fig. 10 Numerical results of stress and strain for jointed coal with REV size after triaxial compression with loading perpendicular to face cleats. *X*-d and *Z*-d refer to the *X*- and *Z*-directions, respectively

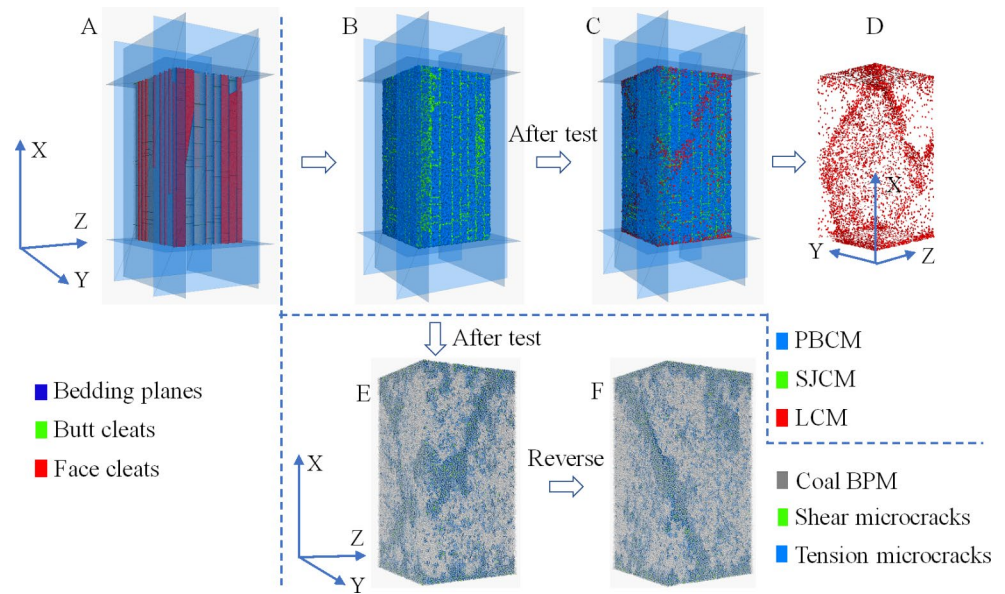


the confining pressure increases to 10 MPa, the TCS continues to increase, and the axial stress tends to be stable after the TCS has been reached, which implies that the specimen is in a plastic-flow state, as shown in Fig. 13d. The estimated transiting pressure of brittleness to ductility for jointed coal in this study is 10 MPa. The elastic modulus also increases with the confining pressure.

The numerical deformation results under different confining pressures are shown in Fig. 15. When there is no confining pressure, the coal specimen has a short-term volume compression stage at the beginning of loading and recovers to the initial volume when the stress is extremely low (0.2 MPa), after which it rapidly expands to 1.2 times the original volume (Fig. 15a). The volumetric strain arises from the lateral strain, indicating that a severe lateral deformation

occurred in the coal specimen, as shown in Fig. 13a. When the confining pressure rises to 1 and 5 MPa, the coal specimens both exhibit an evident volume compression stage and recover to the initial volume in the post-peak stage of axial stress (Fig. 15b and c). When the confining pressure is increased to 10 MPa, the degree of volume compression increases with loading for the coal specimen, and the volumetric strain reaches a maximum value near the stress peak (Fig. 15d). In the subsequent loading, the volumetric strain of the coal specimen remains unchanged, indicating that the axial compression deformation and lateral expansion deformation have reached a dynamic equilibrium, which is the state of plastic flow, shown in Fig. 13d.

Fig. 11 Joint geometry and rupture surface for jointed coal with REV size subjected to numerical triaxial compression with loading perpendicular to butt cleats



4 Discussion

4.1 Joint effect on triaxial compression behavior of jointed coal

The numerical results of the intact coal and jointed coal under different loading orientations with a 1 MPa confining pressure are compared in a histogram (Fig. 16). As illustrated in Fig. 16, the properties of the jointed coal differ from those of the intact coal, which indicates a strong joint effect on the triaxial compression behavior of jointed coal. The joint effect can be summarized as follows:

(1) Joints weaken the peak strength, elastic modulus, and residual strength of the jointed coal under triaxial compression loading. Compared with loading on intact coal, the peak strength, elastic modulus, and residual strength of the jointed coal decrease remarkably (Fig. 15a, b, and c). The peak strengths and elastic moduli are similar for jointed coal with different joint geometries, respectively (Fig. 15a and b), whereas the residual strengths are different (Fig. 15c). Thus, the joint geometry has a significant influence on the post-peak behavior, but little effect on the pre-peak behavior at low confining pressure.

(2) Joints reduce the lateral deformation of jointed coal under triaxial compression loading. The Poisson's ratios of jointed coal are lower than those of intact coal (Fig. 15d), and the lateral strains of jointed coal are lower than those of intact coal at the same axial strain of 2.0% (Fig. 15e). This trend is distinctly different from that under uniaxial compression (Wang et al. 2018), where the lateral deformation of jointed coal is significantly larger than that of intact coal, but consistent with that under direct shear loading (Wang et al. 2019). All fractures are matrix fractures in intact coal

under confining pressure, but the fractures in jointed coal consist of both activated joints and matrix fractures. The dilation of a matrix fracture is larger than an activated joint because of the inherent roughness of the interface surfaces in the matrix fracture and the smooth behavior of the activated joint. Therefore, the lateral deformations and the Poisson's ratio of jointed coal are lower than intact coal under triaxial compression loading.

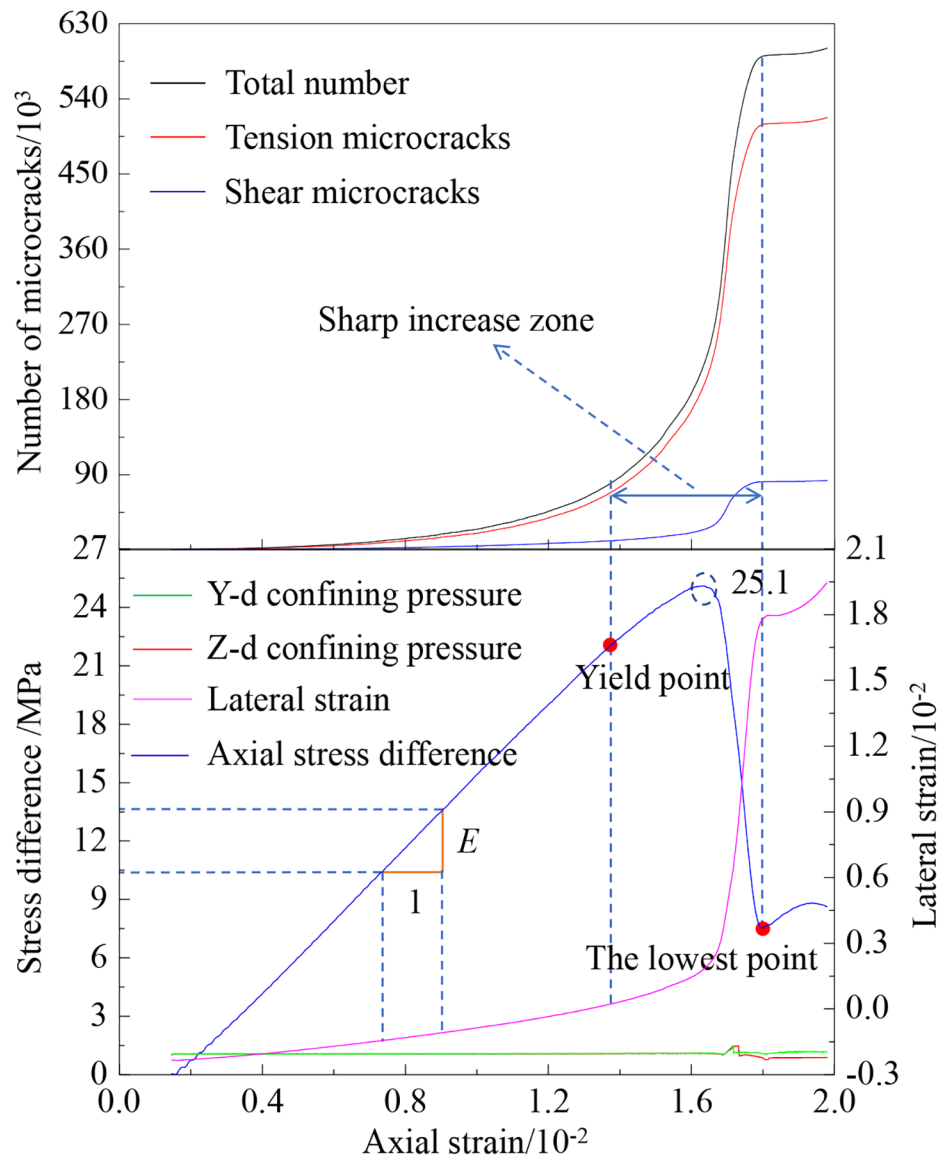
(3) Joints affect the geometries of the shear-rupture surface for jointed coal under triaxial compression loading. The geometries of the shear-rupture surface differ for intact coal and jointed coal under different loading orientations (Figs. 5, 7, 9 and 11), which indicates that the formation of a shear-rupture surface is affected by the joint distribution.

4.2 Confining-pressure effect on triaxial compression behavior of jointed coal

The strengths of intact coal and jointed coal with a REV size without and with a 1 MPa confining pressure are compared in Table 3. Without a confining pressure, the average strength of the jointed coal is 13.1 MPa less than that of intact coal, but the strength difference decreases to 7.2 MPa when the confining pressure increases to 1 MPa. The strength difference will decrease further with an increase in confining pressure. Therefore, the influence of joints on the triaxial compression behavior of jointed coal will decrease and even disappear with confining pressure.

According to an analysis of the numerical triaxial-compression results for jointed coal under different confining pressures in Sect. 3.3, the triaxial compression behavior of jointed coal also has a strong confining-pressure effect. As the confining pressure increases, the following responses of

Fig. 12 Numerical results of stress and strain for jointed coal with REV size after triaxial compression with loading perpendicular to butt cleats. *Y*-d and *Z*-d refer to the *Y*- and *Z*-directions, respectively



jointed coal are observed: (1) the peak strength and residual strength increase significantly (Fig. 14); (2) the elastic modulus increases, especially at a low confining pressure (Fig. 14); (3) the stress drop in the post-peak stage decreases and even disappears (Fig. 14); (4) the mechanical behavior transitions from brittleness to ductility (Fig. 14); (5) the volume deformation transitions from expansion to compression (Fig. 15); (6) the failure mode transitions from shear-rupture surface to plastic flow (Figs. 13 and 15); (7) the influence of joints on the triaxial compression behavior decreases and even disappears (Table 3).

4.3 Failure mechanism of jointed coal subjected to triaxial compression

In the triaxial compression tests, the interaction of confining pressure and axial loading stress result in shear stress in the jointed-coal specimen, which leads to the formation of shear-rupture surfaces. Shear-rupture surfaces have been found in almost all triaxial compression tests, except for the one with 10 MPa confining pressure. The joints distribution and confining pressure will affect the formation of the shear-rupture surface in triaxial compression tests.

For the jointed rock, joints parallel to the loading direction can be activated easily by shear sliding and dilation without confining pressure. However, the joints' activation becomes more difficult with an increase in the confining

Fig. 13 Fracture geometries of jointed coal after triaxial loading under four magnitudes of confining pressure. The numerical result without confining pressure is cited from Wang et al. (2018)

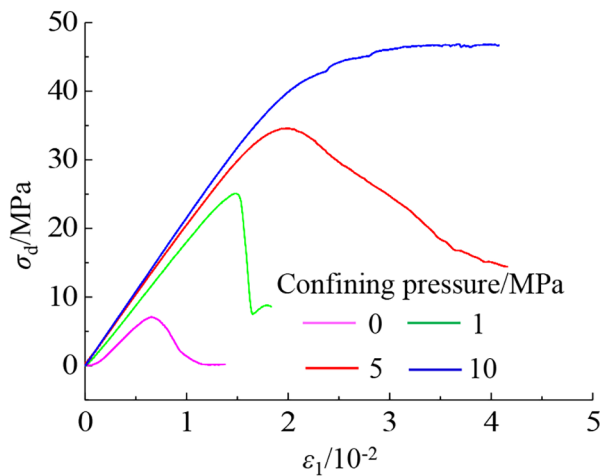
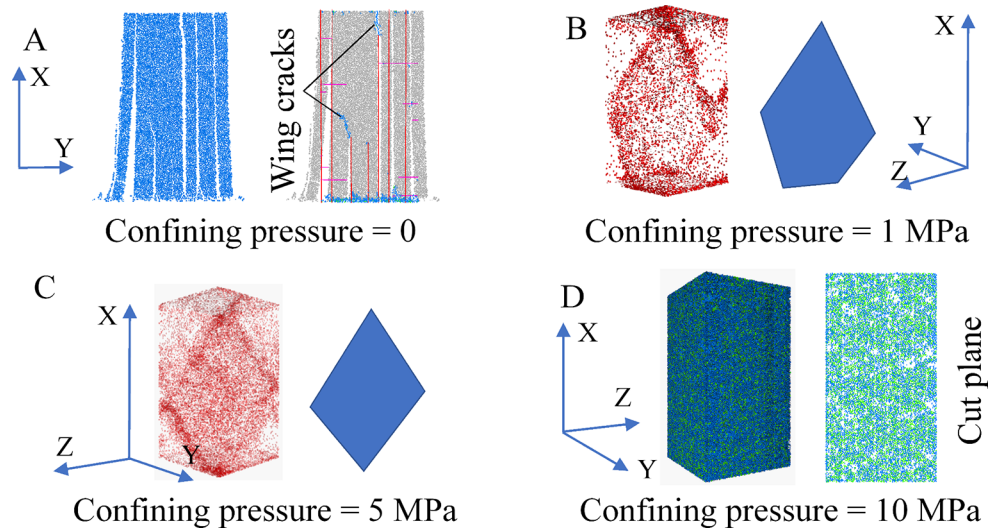


Fig. 14 Numerical strength results of jointed coal subjected to triaxial compression with different confining pressures. Notes: σ_d refers to the difference between axial stress and confining pressure; ϵ_1 denotes the axial strain

pressure. This can be verified by the joints' activation ratios of jointed coal under different confining pressures (Fig. 17). When there is no confining pressure, 91.9% of pre-existing joints were activated to fractures, which indicates that the jointed coal fails along joints under triaxial loading without confining pressure (i.e., uniaxial compression loading). When the confining pressure increases to 1 and 5 MPa, although there is a sharp decrease in the joints activation ratio, there are still some joints activated to fractures. The activated joints will significantly affect the geometry of shear-rupture surface, which is why the geometries of the shear-rupture surfaces vary in different tests. When the confining pressure rises to 10 MPa, only 2.1% of joints are activated to fractures, which indicates that the influence of joints on the failure of jointed coal can be ignored at a high

confining pressure. Instead of the activated joints, numerous microcracks grow between the rock particles throughout the coal specimen under high confining pressure, indicating that plastic-flow failure occurs.

5 Conclusions

We employed the SRM approach to investigate the triaxial compression behavior of large-scale jointed coal. A series of triaxial compression tests under different loading orientations and confining pressures were conducted numerically to obtain the joint and confining-pressure effects on triaxial compression behavior and reveal the failure mechanism of jointed coal. The jointed coal fails by means of shear-rupture surface under triaxial compression loading with a confining pressure (not too high), and the geometries of shear-rupture surface are affected by the joints' distribution. We defined and evaluated the joints activation in different numerical tests and found that the influence of joints on the triaxial compression behavior of jointed coal decreases and even disappears with confining pressure. The failure mode of plastic flow for jointed coal subjected to triaxial compression loading under a high confining pressure was realized numerically. This study helps deepen the understanding of the triaxial compression behavior of jointed rock mass with a large scale. For a heavily jointed rock mass subjected to triaxial compression, we provide a rational prediction for its potential failure mode under different confining pressures. It is not necessary to excessively consider the influence of existing joints when evaluating the mechanical properties of jointed rock mass under high confining pressure.

Fig. 15 Numerical deformation results of jointed coal subjected to triaxial compression with different confining pressures. σ_d refers to the difference between axial stress and confining pressure; ε , ε_1 , ε_2 and ε_v refer to the strain, axial strain, lateral strain and volumetric strain, respectively

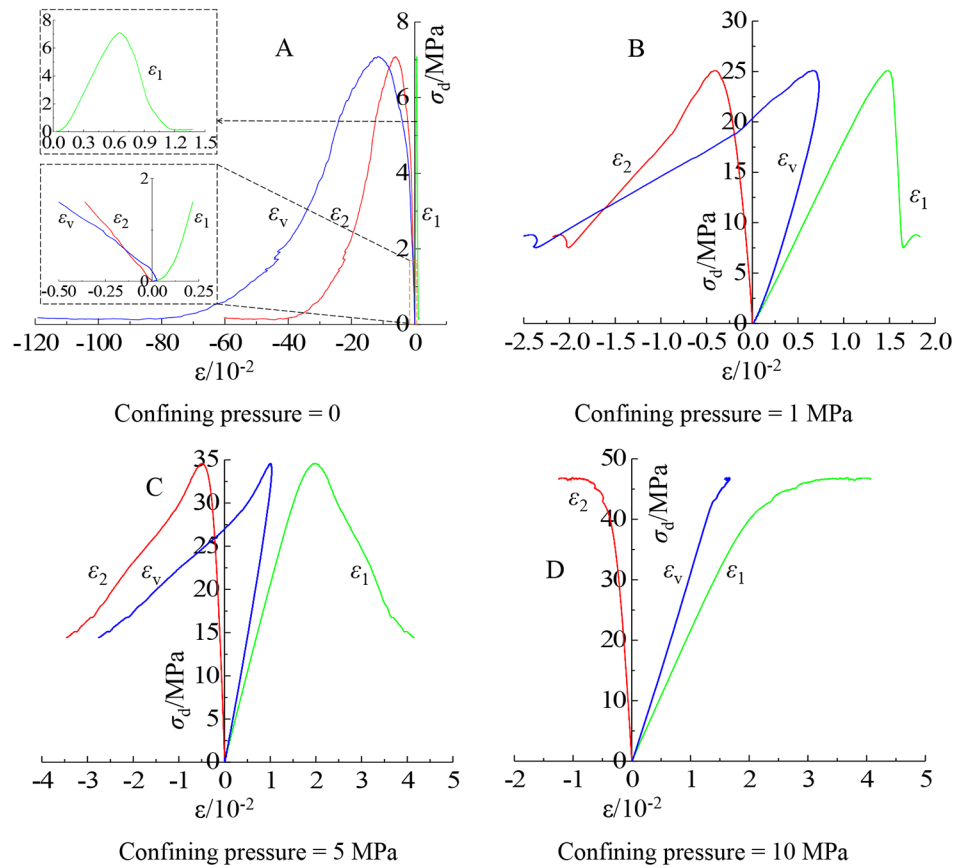


Fig. 16 Numerical results of intact coal and jointed coal with a REV size under different triaxial loading orientations with 1 MPa confining pressure. RS refers to residual strength; ν refers to Poisson's ratio; Ls refers to lateral strain

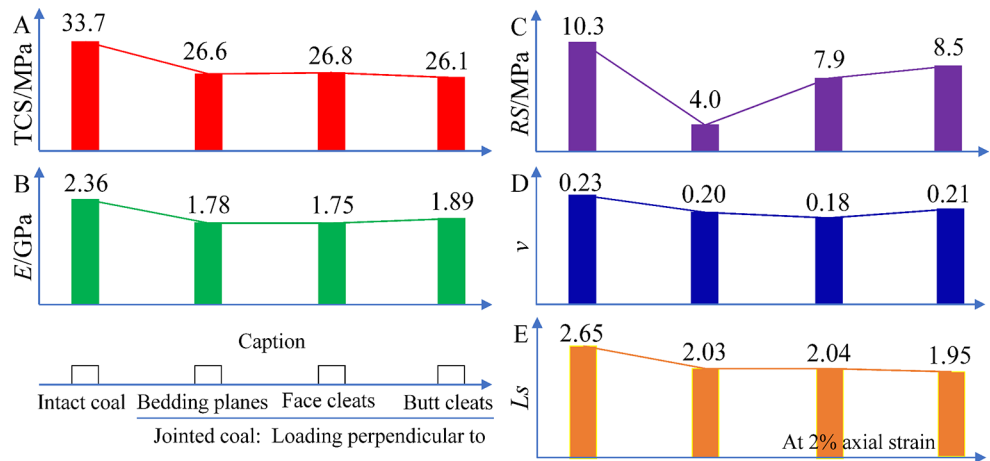


Table 3 Strength comparison between intact coal and jointed coal with and without 1 MPa confining pressure

Confining pressure (MPa)	Strength of intact coal (MPa)	Strength of jointed coal with loading perpendicular to				Difference in strengths
		Bedding planes	Face cleats	Butt cleats	Average	
0	23.1	15.3	7.7	7.1	10.0	13.1
1	33.7	26.6	26.8	26.1	26.5	7.2

Note: Difference in strengths refers to the strength difference between intact and jointed coal. The numerical results of coal without confining pressure are cited from Wang et al. (2018)

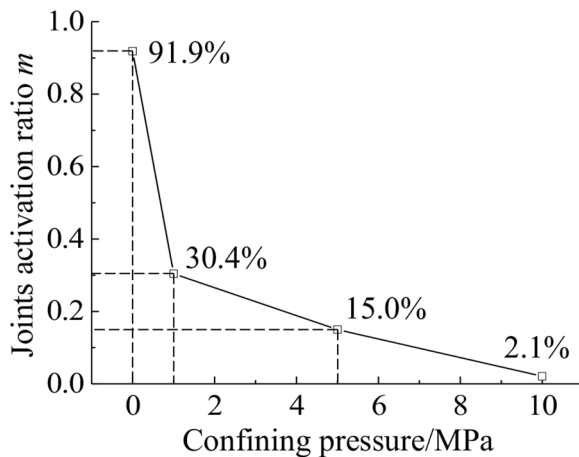


Fig. 17 Joints activation ratio of jointed coal subjected to triaxial compression with different confining pressures

Acknowledgements This work has been supported by the National Nature Science Foundation of China (51904153), and funding of Tiandi Science & Technology Co Ltd (2022-2-TD-QN008, KJ-2019-TDKCSYS-01).

Open Access This article is licensed under a Creative Commons Attribution 4.0 International License, which permits use, sharing, adaptation, distribution and reproduction in any medium or format, as long as you give appropriate credit to the original author(s) and the source, provide a link to the Creative Commons licence, and indicate if changes were made. The images or other third party material in this article are included in the article's Creative Commons licence, unless indicated otherwise in a credit line to the material. If material is not included in the article's Creative Commons licence and your intended use is not permitted by statutory regulation or exceeds the permitted use, you will need to obtain permission directly from the copyright holder. To view a copy of this licence, visit <http://creativecommons.org/licenses/by/4.0/>.

References

- Bahaaddini M, Sharrock G, Hebblewhite BK (2013) Numerical direct shear tests to model the shear behaviour of rock joints. *Comput Geotech* 51:101–115
- Barton N, Lien R, Lunde J (1974) Engineering classification of rock masses for the design of tunnel support. *Rock Mech* 6(4):189–236
- Bewick RP, Kaiser PK, Bawden WF, Bahrani N (2014) DEM simulation of direct shear: 1. rupture under constant normal stress boundary conditions. *Rock Mech Rock Eng* 47:1647–1671
- Bieniawski ZT (1968a) The effect of specimen size on compressive strength of coal. *Int J Rock Mech Min Sci* 5:325–335
- Bieniawski ZT (1968b) In situ strength and deformation characteristics of coal. *Eng Geol* 2(5):325–340
- Bieniawski ZT (1973) Engineering classification of jointed rock masses. *Civil Eng South Africa* 15(12):335–343
- Chen YL, Zuo JP, Liu DJ, Li YJ, Wang ZB (2021) Experimental and numerical study of coal-rock biomaterial composite bodies under triaxial compression. *Int J Coal Sci Technol* 8(5):908–924
- Cook NGW, Hodgson K, Hojem JPM (1971) A 100 MN jacking system for testing coal pillars underground. *J S Afr Inst Min Metall* 71:215–224
- Dou LT, Yang K, Chi XL (2021) Fracture behavior and acoustic emission characteristics of sandstone samples with inclined precracks. *Int J Coal Sci Technol* 8(1):77–87
- Dron RW (1925) Notes on cleat in the Scottish coalfield. *Trans Inst Min Eng* 70:115–117
- Gao FQ, Stead D, Kang HP (2014) Numerical investigation of the scale effect and anisotropy in the strength and deformability of coal. *Int J Coal Geol* 136:25–37
- Head D, Vanorio T (2016) Effects of changes in rock microstructures on permeability: 3D printing investigation. *Geophys Res Lett* 43(14):7494–7502
- Hoek E (1994) Strength of rock and rock masses. *ISRM News J* 2(2):4–16
- Hoek E, Brown ET (1980) Empirical strength criterion for rock masses. *J Geotech Geoenviron* 106:1013–1035
- Hoek E, Brown ET (1997) Practical estimates of rock mass strength. *Int J Rock Mech Min Sci* 34(8):1165–1186
- Huang YH, Yang SQ, Zhao J (2016) Three-dimensional numerical simulation on triaxial failure mechanical behavior of rock-like specimen containing two unparallel fissures. *Rock Mech Rock Eng* 49(12):4711–4729
- Itasca Consulting Group Inc (2016) PFC3D (Particle Flow Code in 3 Dimensions) manual, version 5.0. Minneapolis, Minnesota
- Ivars DM, Pierce ME, Darcel C, Reyes-Montes J, Potyondy DO, Young RP, Cundall PA (2011) The synthetic rock mass approach for jointed rock mass modelling. *Int J Rock Mech Min Sci* 48:219–244
- Jiang C, Zhao GF, Zhu JB, Zhao YX, Shen LM (2016) Investigation of dynamic crack coalescence using a gypsum-like 3D printing material. *Rock Mech Rock Eng* 49(10):1–16
- Jiang Q, Song LB (2018) Application and prospect of 3D printing technology to physical modeling in rock mechanics. *Chin J Rock Mech Eng* 37(1):23–36
- Kang TH, Jin ZM, Zhao YS (1994) Study of the structural features and the distribution rules of the cracks in coal mass. *J Xi'an Min Inst* 14(4):318–323
- Kendall PE, Briggs H (1933) The formation of rock joints and the cleat of coal. *Proc R Soc Edinburgh* 53:164–187
- Kim BH, Walton G, Larson MK, Berry S (2021) Investigation of the anisotropic confinement-dependent brittleness of a Utah coal. *Int J Coal Sci Technol* 8(2):274–290
- Laubach SE, Marrett RA, Olson JE, Scott AR (1998) Characteristics and origins of coal cleat: a review. *Int J Coal Geol* 35:175–207
- Potyondy DO, Cundall PA (2004) A bonded-particle model for rock. *Inter J Rock Mech Min Sci* 41:1329–1364
- Su XB, Feng YL, Chen JF, Pan JN (2001) The characteristics and origins of cleat in coal from Western North China. *Int J Coal Geol* 47(1):51–62
- Van Heerden WL (1975) In situ complete stress–strain characteristics of large coal specimens. *J S Afr Inst Min Metall* 75:207–217
- Walton G, Alejano LR, Arzua J, Markley T (2018) Crack damage parameters and dilatancy of artificially jointed granite samples under triaxial compression. *Rock Mech Rock Eng* 51(6):1637–1656
- Wang XQ, Kang HP, Gao FQ (2019) Numerical investigation on the shear behavior of jointed coal mass. *Comput Geotech* 106:274–285
- Wang XQ, Kang HP, Gao FQ, Zhao K (2018) DEM simulation of mechanical behavior of jointed coal in large scale under uniaxial compression. *J China Coal Soc* 43(11):3088–3097
- Wang XQ, Kang HP, Zhao K, Liu YD (2016) Numerical analysis of bonding stiffness for support effectiveness of pre-stressed bolts. *J Chin Coal Soc* 41(12):2000–2007
- Xiao WM, Deng RG, Fu XM, Wang CY (2015) Experimental study of deformation and strength properties of simulated columnar

- jointed rock masses under conventional triaxial compression. *Chin J Rock Mech Eng* 34(1):2817–2826
- Yang SQ, Lu JW, Tian WL, Tang JZ (2018) Experimental study of mechanical behavior of rock specimens with different joint roughness coefficient under conventional triaxial compression. *Rock Soil Mech* 39(1):21–32
- Zhou Y, Wu SC, Gao YT, Misra A (2014) Macro and meso analysis of jointed rock mass triaxial compression test by using equivalent rock mass (ERM) technique. *J Cent South Univ* 21(3):1125–1135

Publisher's Note Springer Nature remains neutral with regard to jurisdictional claims in published maps and institutional affiliations.